DATA PAPER OPEN ACCESS

Data Paper: E-Defense Shake-Table Tests on a Steel Moment-Resisting Frame Supplemented With Spines and Force-Limiting Connections

Yi Qie[1] | Bryam Astudillo[2] | Jessica Duncan[3] | Zhuoqi Tao[4] | Taichiro Okazaki[5] | Larry Fahnestock[4] | Richard Sause[3] | James Ricles[3] | Barbara Simpson[2] | Masahiro Kurata[6] | Yohsuke Kawamata[7] | Kohei Hattori[8]

[1]Graduate School of Engineering, Hokkaido University, Sapporo, Hokkaido, Japan | [2]Department of Civil and Environmental Engineering, Stanford University, Stanford, California, USA | [3]Department of Civil and Environmental Engineering, Lehigh University, Bethlehem, Pennsylvania, USA | [4]The Grainger College of Engineering, Department of Civil and Environmental Engineering, University of Illinois Urbana-Champaign, Urbana, Illinois, USA | [5]Faculty of Engineering, Hokkaido University, Sapporo, Hokkaido, Japan | [6]Disaster Prevention Research Institute, Kyoto University, Uji, Kyoto, Japan | [7]Hyogo Earthquake Engineering Research Center, National Research Institute for Earth Science and Disaster Resilience, Miki, Hyogo, Japan | [8]BrainPad Inc. (Former Waseda University), Minato-ku, Tokyo, Japan

Correspondence: Yi Qie (tsinghuaqyyx@gmail.com)

Received: 15 April 2025 | **Revised:** 25 May 2025 | **Accepted:** 11 June 2025

Funding: This work was supported by National Science Foundation (CMMI 1928906, CMMI 1926326, CMMI 1926365). American Institute of Steel Construction, Nippon Steel, Nippon Steel Engineering Co. Ltd, Nippon Steel Metal Products Co. Ltd, Disaster Prevention Research Institute, Kyoto University, Japan Society for the Promotion of Science (20H00269), National Research Institute for Earth Science and Disaster Prevention.

Keywords: data | higher modes | nonlinear response | shake-table test | spine | steel building

ABSTRACT

This data paper presents data obtained from E-Defense shake-table tests of a full-scale, steel moment-resisting frame (MRF) supplemented with Spines. Herein, the Spines were pin-based columns with sufficient stiffness and strength to distribute plastic deformation evenly over the height of the MRF. The specimen was tested under two configurations: first, with the Spine rigidly connected to the MRF; second, with the Spine connected to the MRF through force-limiting connections (FLCs). Each specimen configuration underwent earthquake simulations using ground motions with two scale factors. The tests demonstrated the expected benefits of Spines as well as the disadvantage of inducing large floor accelerations in the structure and large shear forces in the Spines. The tests also demonstrated how the FLCs can mitigate these disadvantages. This data paper reports an overview of the tests, data archive structure, and potential use of the data. The data can be used, for example, to reproduce the observations presented by the authors, to compare the dynamic response of the specimen with building specimens tested in other shake-table test programs, to validate numerical models against the measured specimen response, or to formulate classroom exercises on system identification of linear and nonlinear systems.

1 | Introduction

A Spine is defined as a vertically continuous multi-story structural element designed to remain essentially elastic, while other components of the seismic force-resisting system yield, thereby imposing more uniform story deformations and yielding across the height of a conventional seismic force-resisting system (SFRS), such as a moment-resisting frame (MRF) or concentrically braced frame (CBF), referred to generically as "Frame" herein. Spines can come in various configurations, such as pin-supported walls [1], spine core frames [2], rocking cores or walls [3], and strong-back braced frames [4, 5]. In this research, the Spines are stiff pin-based

columns designed to remain elastic. Spines with pinned bases avoid increasing the overturning moment capacity and the related first mode response of the structure, relative to the overturning moment resistance of the Frame alone.

The benefits of Spines to mitigate story mechanisms and to utilize the full energy-dissipation potential of the Frame are intuitive. However, Spines can induce large floor accelerations in the structure and draw large shear force demands into the Spines themselves. Wu et al. [6] and Simpson [7], among others, noted that frames supplemented with spines tend to have near-elastic higher-mode responses, which produce the above-mentioned demands. Since Spines are designed to remain elastic, there is no yielding mechanism to limit the inertial forces from the higher-mode responses.

The large acceleration induced by Spines may be mitigated by introducing deformable connections between the Spines and Frame, assuming that most of the mass of the structure is directly attached to the Frame and little mass is associated with the Spines [8]. In this research, these deformable connections are termed force-limiting connections (FLCs). Use of FLCs was explored previously in a half-scale shake-table test by Zhang et al. [9] of a reinforced-concrete structure comprising shear walls and a gravity system connected by FLCs in the form of buckling-restrained braces (BRBs) and friction dampers. The structure tested by Zhang et al. [9] was significantly different from the structure tested in the present study, since the gravity system (which supported almost all of the mass) of the structure tested by Zhang et al. [9] provided almost no overturning moment resistance and the shear walls provided almost all of the overturning moment resistance; the Frame (with almost all of the mass) of the structure used in the present study provided all of the overturning moment resistance and the pin-based Spines provided no overturning moment resistance. As a consequence of this difference, the FLCs of the structure tested by Zhang et al. [9] transmitted both first-mode forces and higher mode forces to the shear walls and were intended to have substantial deformation capacity, while the FLCs of the structure used in the present research transmitted smaller forces and did not require substantial deformation capacity.

The present study was undertaken to generate valuable data on the seismic response of Frame–Spine systems with and without FLCs. The shake table tests were conducted in December 2020 at E-Defense in Japan. The project was a major U.S.–Japan collaboration, including the University of Illinois Urbana-Champaign, Lehigh University, Oregon State University, and Stanford University from the U.S. and Kyoto University, Hokkaido University, and National Research Institute for Earth Science and Disaster Resilience (NIED) from Japan. This paper describes the data obtained from the project including the test plan, data structure, data reliability, and examples of potential use. Other information about the project can be found in Fahnestock et al. [10] and Astudillo et al. [11]. Raw data collected from the shake-table tests are available at the NIED E-Defense test data archive (ASEBI https://asebi.bosai.go.jp/). A more complete data set obtained from the project, which is the subject of this data paper, is published in DesignSafe Cyberinfrastructure [12] by Fahnestock et al. [13].

2 | Data Overview

The data set was obtained from unidirectional shake-table tests of a full-scale building specimen comprising a steel MRF, a pair of vertical Spines, and FLCs. The four-story steel MRF had a weak first story and large masses at the top two stories to excite higher vibration modes. The data provide unique experimental evidence on how the Spines affect the post-elastic dynamic response of the MRF and how the FLCs might alter that dynamic response. The specimen was tested in two configurations: first, the Spines were connected to the MRF by bolted connections; second, the Spines were connected to the MRF through FLCs. The specimen was subjected to the same ground motions in both configurations to understand how the FLCs may affect the characteristics of MRF with Spines. In total, the specimen was subjected to six primary motions, which were two recorded ground motions amplified to different intensities, and eight white-noise excitations to characterize the change in dynamic properties as damage accumulated.

Details of the specimen are provided, including drawings and construction photos. Data on specimen response was obtained from 174 instruments and 208 channels placed for the purpose of the tests, in addition to acceleration, velocity, and displacement response of the shake table. The instruments were placed to allow deduction of dynamic properties, force versus deformation hysteresis per story, and for individual members or components, and force distribution in the MRF. Twenty-three video feeds document the global response of the system and the local response of selected components, such as connections (bolted or FLC) between the MRF and Spine, and column panel zones. Archived photos present the construction and demolition process, the initial state, and damage accumulation in primary members and components.

Numerical data obtained at a fixed time interval were stored in text files. The raw data was examined to identify failures and errors in the measured signals. Errors were corrected to the extent possible. All targeted responses could be deduced, although compromise in accuracy was noted for some responses affected by signal loss beyond a certain instant during the tests. The data set includes raw data, data processed to different stages, as well as deduced physical responses such as member section force, floor acceleration, story drift ratio, etc. Videos and photos are available to correlate the hysteretic response with visual images.

The data can be used, for example, to reproduce observations presented in articles published from the project, to examine the specimen response in further detail than described in the authors' publications, to validate numerical models against the measured specimen response, to train AI models, to compare the dynamic response of the specimen with building specimens tested in other shake-table test programs, to formulate classroom exercises on system identification of linear and nonlinear systems, and to form the scientific basis for new design code development.

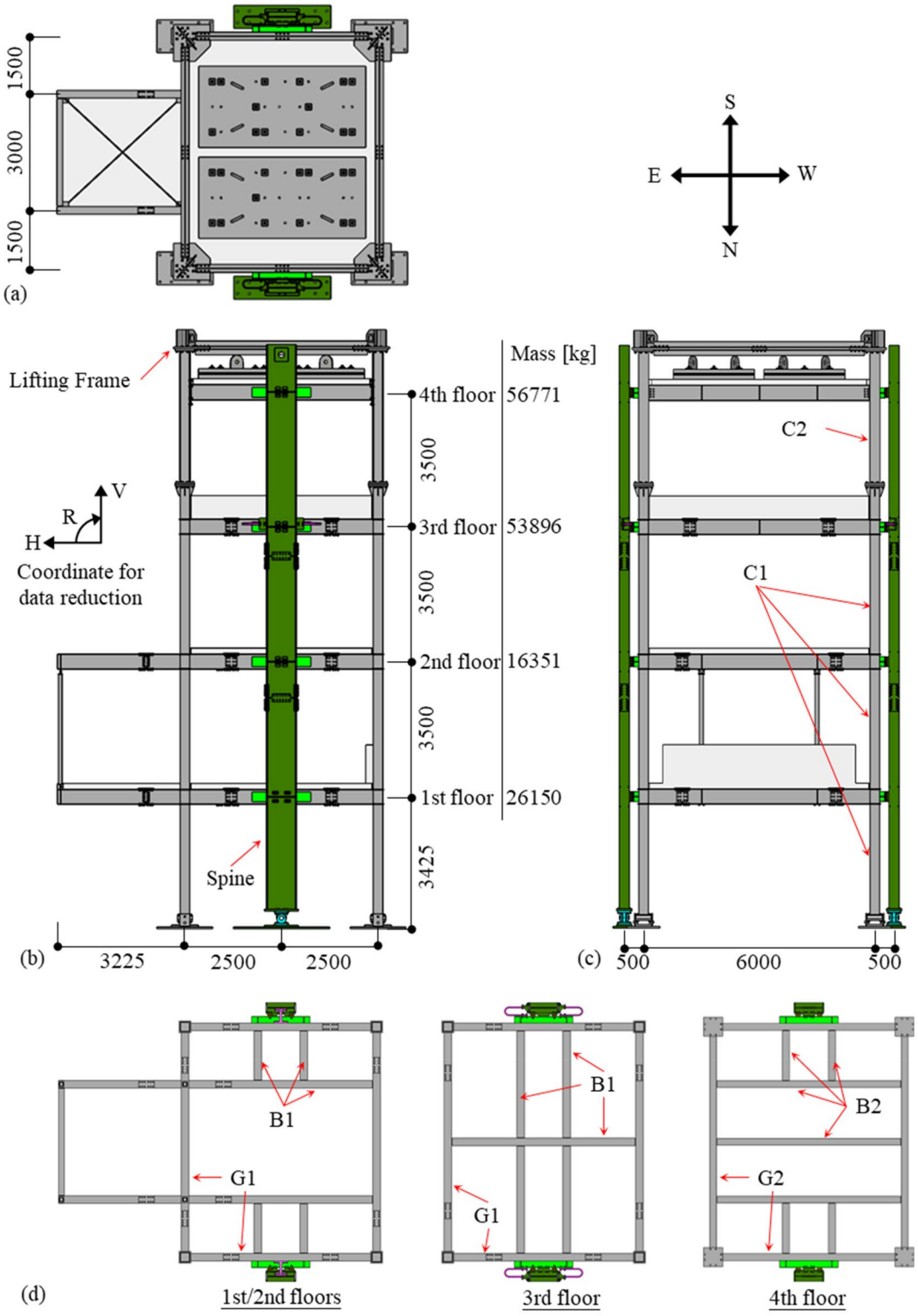

FIGURE 1 | Specimen layout: (a) fourth-floor plan, (b) North elevation, (c) West elevation, and (d) floor beam arrangement [units: mm].

3 | Test Specimen

The specimen was a full-scale, steel structure comprising three parts: (1) a four-story, 1-by-1 bay, steel MRF, (2) two Spines, one at the South and one at the North side of the MRF, and (3) connections between the MRF and Spine at each floor. The specimen was designed for unidirectional tests only. Figure 1 shows the structural layout and Figure 2 shows photos of the specimen.

The columns of the MRF were pinned at the base to enforce a weak first story.

The lower three stories of the MRF were adapted from a base-isolated hospital building specimen tested for the Tokyo Metropolitan Resilience Project [14]. The MRF was formed by modifying the original MRF column bases from fixed to pinned and adding a fourth story. Consequently, the first to third stories

of the MRF used Japanese materials, while the fourth-story columns and roof beams used U.S. materials. Figure 3 shows the nominal dimensions of the primary steel sections and the FLCs utilized in testing. Table 1 lists measured and nominal tension properties of the test specimen, where the latter is bracketed. Reinforced-concrete floor slabs were cast on all floors using flat-on-top folded steel deck, with shear studs designed to develop fully composite action. The compressive strength of the concrete

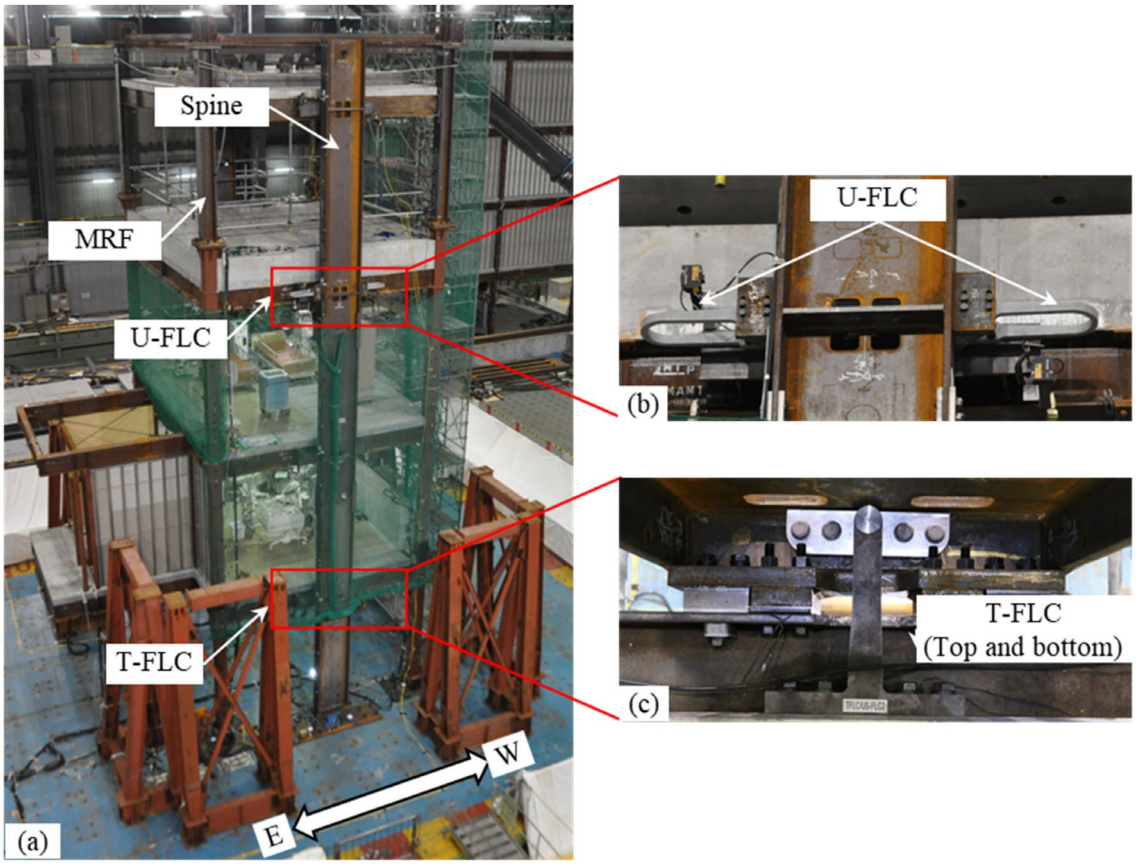

FIGURE 2 | Specimen photos: (a) specimen viewed from North–East, (b) close-up view of two U-FLCs from side, and (c) close-up view of upper T-FLCs from above.

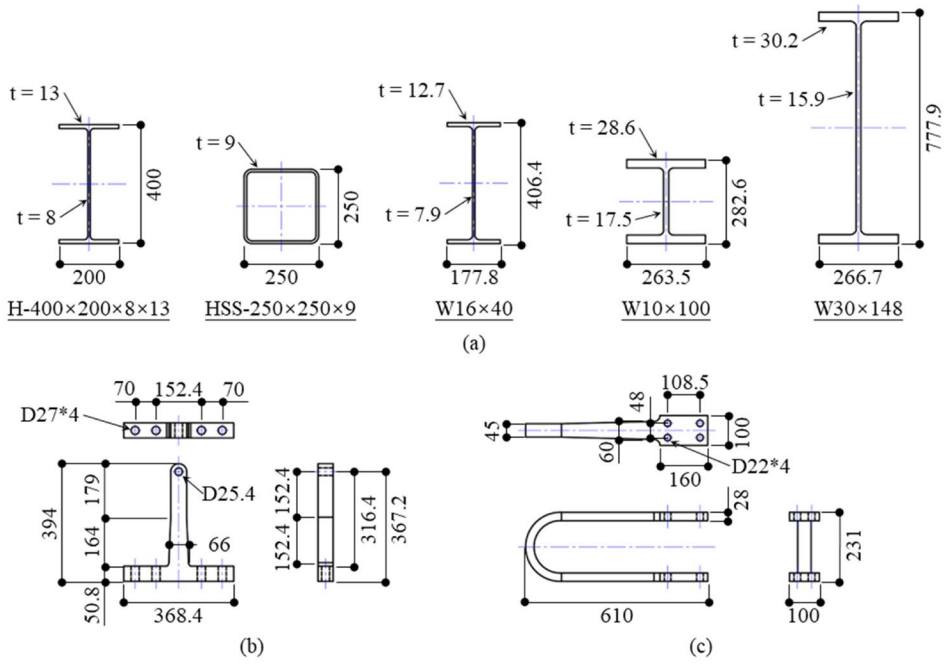

FIGURE 3 | Nominal member dimensions: (a) steel sections, (b) T-FLC, and (c) U-FLC [units: mm].

was established from standard cylinder tests conducted 28 days after casting, resulting in 47 N/mm^2 for the first and third floors, 37 N/mm^2 for the second floor, and 35 N/mm^2 for the fourh floor. Foam was placed between the RC slab and column surface to prevent force transfer by direct bearing. The Spines were deep girders, to be stiff in flexure, pinned at the base and connected to the MRF at each floor by connections located at the midspan of the MRF beams. As indicated by the floor mass distribution in Figure 1b, the masses of the top two floors were increased by adding a thicker concrete slab, weighing 36 789 kg, at the third floor, and by adding steel plates, totaling 36 875 kg, fastened to the floor slab by posttensioned bars, at the fourth floor. The beams at third and fourth floors were provided with enough shear studs to transfer the extra inertia developed through the larger mass.

As shown in Figure 4, two different connection configurations were applied between the MRF and Spines at each floor: bolted connections and FLCs. The former set of connections was used to form an MRF–Spine system with negligible shear deformation in the connections, and the latter set of connections was used to form an MRF–Spine–FLC system. The connections were designed to enable conversion from bolted connections to FLCs in a single day. At each connection, a stiffening beam was bolted to the MRF beam, and a thick connection plate was welded to the Spine at the corresponding location. Each connection included a mechanism that constrained out-of-plane motion and twisting of the Spine with respect to the MRF beam. The mechanism comprised four structural bolts (Japanese Industry Standard grade F10T) connecting the MRF beam (at the stiffening beam) and the Spine (at the thick connection plate) that permitted relative slip with a small slip coefficient secured by Teflon applied at compressed contact surfaces and graphite sprayed at the tensioned contact surfaces. A pair of T-FLCs [15] was set at the first floor, and a pair of U-FLCs (UD-40 damper from Nippon Steel Engineering) was set at the third floor. Furthermore, the bolted connections in the MRF–Spine system, shown in Figure 4b, had the Spine fastened to the MRF by structural bolts (F10T). In the MRF–Spine–FLC system shown in Figure 4c, the FLCs were activated when these bolts were removed at all floors except the fourth floor. The structural bolts at the fourth floor kept the Spines stable with respect to the MRF.

TABLE 1 | List of steel members.

Member	Section	Grade	Yield strength [N/mm^2]	Tensile strength [N/mm^2]
C1	HSS-250×250×9	BCR295	361 (295)	431 (400)
G1/B1	H-400×200×8×13	SN490B/SS400	419 (325)	537 (490)
C2	W10×100	ASTM A992	(345)	(448)
G2/B2	W16×40	ASTM A992	(345)	(448)
Spine	W30×148	ASTM A992	(345)	(448)

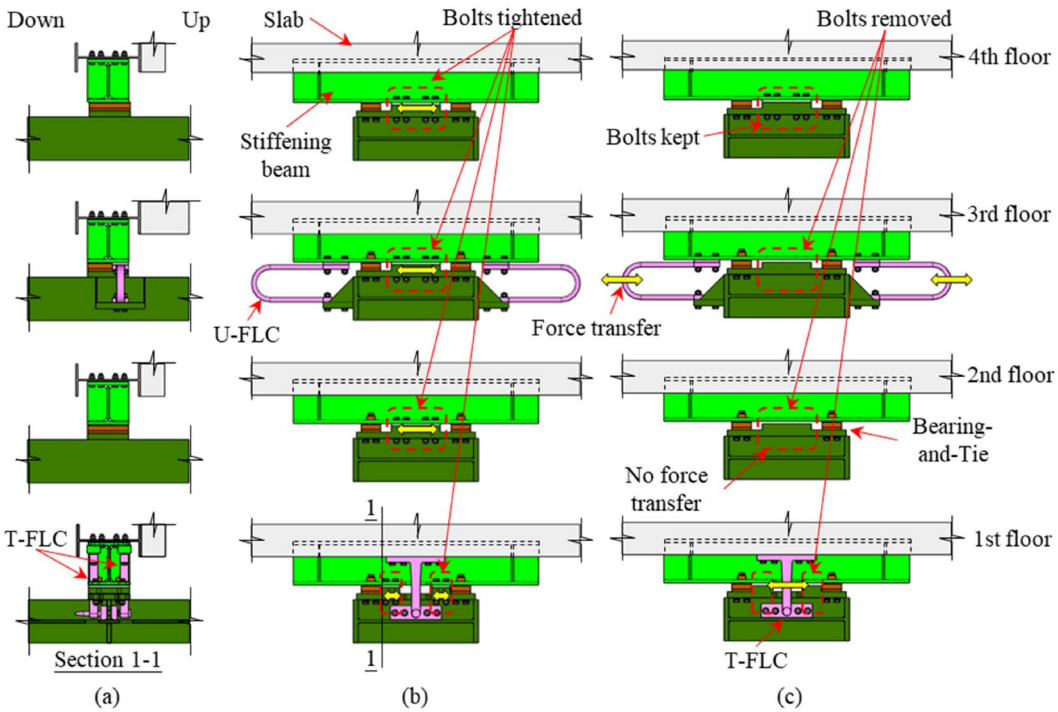

FIGURE 4 | Connection configurations: (a) left view, (b) top view of bolted connections in the MRF–Spine system, and (c) top view of FLCs in the MRF–Spine–FLC system.

4 | Excitations

The project occupied the E-Defense shake table between December 2 and 21 of 2020. The shake-table tests were conducted on December 15 and 17. The tests subjected the specimen to unidirectional excitation in the East–West direction. Table 2 summarizes the excitation cases that included the primary excitations and white noise excitations. The two structural systems, MRF–Spine and MRF–Spine–FLC, were subjected to two ground motions at two different scales for six primary excitations. White noise excitations were conducted before and after each primary excitation.

Figure 5 illustrates the acceleration history of the excitations. The primary excitations were two strong motions scaled to two different scales. One motion was the fault normal component of the Northridge Sepulveda VA Hospital Station record from the 1994 Northridge earthquake (abbreviated hereinafter as Northridge VA), the other was the NS component of the JMA Kobe record from the 1995 Kobe earthquake (abbreviated hereinafter as JMA Kobe). Figure 6 shows the pseudo-acceleration and displacement spectra of the target ground motions and realized shake-table motions. The figure indicates that Northridge VA includes large pseudo-acceleration near the second period of the specimen, while JMA Kobe has larger spectral displacements near the first period. The shake table closely realized the targeted motion over the relevant period range, except for the range below 0.5 s, where the realized motion overshot the target motion, amplifying the second-mode response. The direction of shake-table motion was flipped for Case 07 (Northridge VA 40%) and Case 09 (Northridge VA 100%) to avoid accumulation of story drift. In addition to the recorded strong motions, a synthetic white noise excitation with a flat frequency band of 0.1 to 35 Hz, and root-mean-square intensity of 0.55 m/s^2 was used to enable analysis of the dynamic properties of the specimen before and after each primary excitation. The white noise excitation was scaled down to PGA of 0.5 m/s^2 when applied to the specimen.

5 | Instrumentation Plan

Figures 7 and 8 illustrate the overall instrumentation plan, Table 3 lists the types of instruments used, and Table 4 relates the instrument to the deduced acceleration, force, or displacement response component. Figure 9 shows photos of instrument

TABLE 2 | List of excitations.

Day	Load case	System	Excitation	Scale	PGA [m/s^2]
2020/12/15	01	MRF–Spine	White noise	—	0.5
	02		Northridge VA	40%	3.0
	03		White noise	—	0.5
	04		Northridge VA	100%	7.4
	05		White noise	—	0.5
2020/12/17	06	MRF–Spine–FLC	White noise	—	0.5
	07		Northridge VA (opposite)	40%	3.0
	08		White noise	—	0.5
	09		Northridge VA (opposite)	100%	7.4
	10		White noise	—	0.5
	11		JMA Kobe	50%	4.1
	12		White noise	—	0.5
	13		JMA Kobe	100%	8.2
	14		White noise	—	0.5

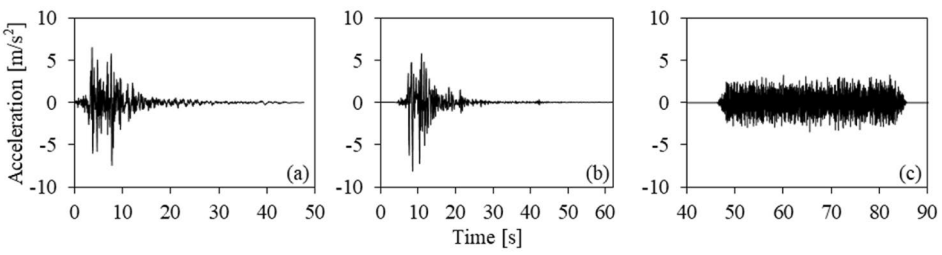

FIGURE 5 | Acceleration history of target ground motions: (a) Northridge VA, (b) JMA Kobe, and (c) white noise (amplitude not adjusted).

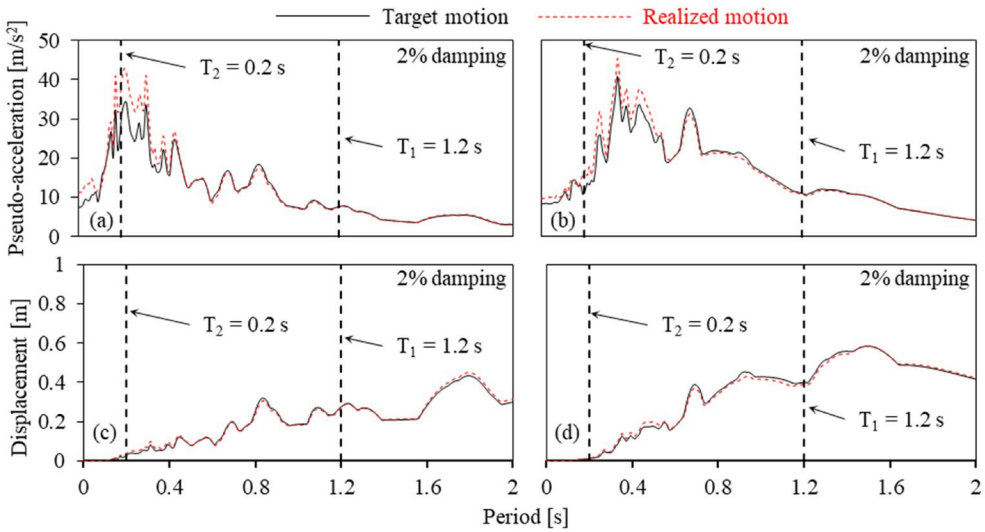

FIGURE 6 | Spectra of excitations with 2% damping: (a) Northridge VA 100%, pseudo-acceleration; (b) JMA Kobe 100%, pseudo-acceleration; (c) Northridge VA 100%, displacement; (d) JMA Kobe 100%, displacement.

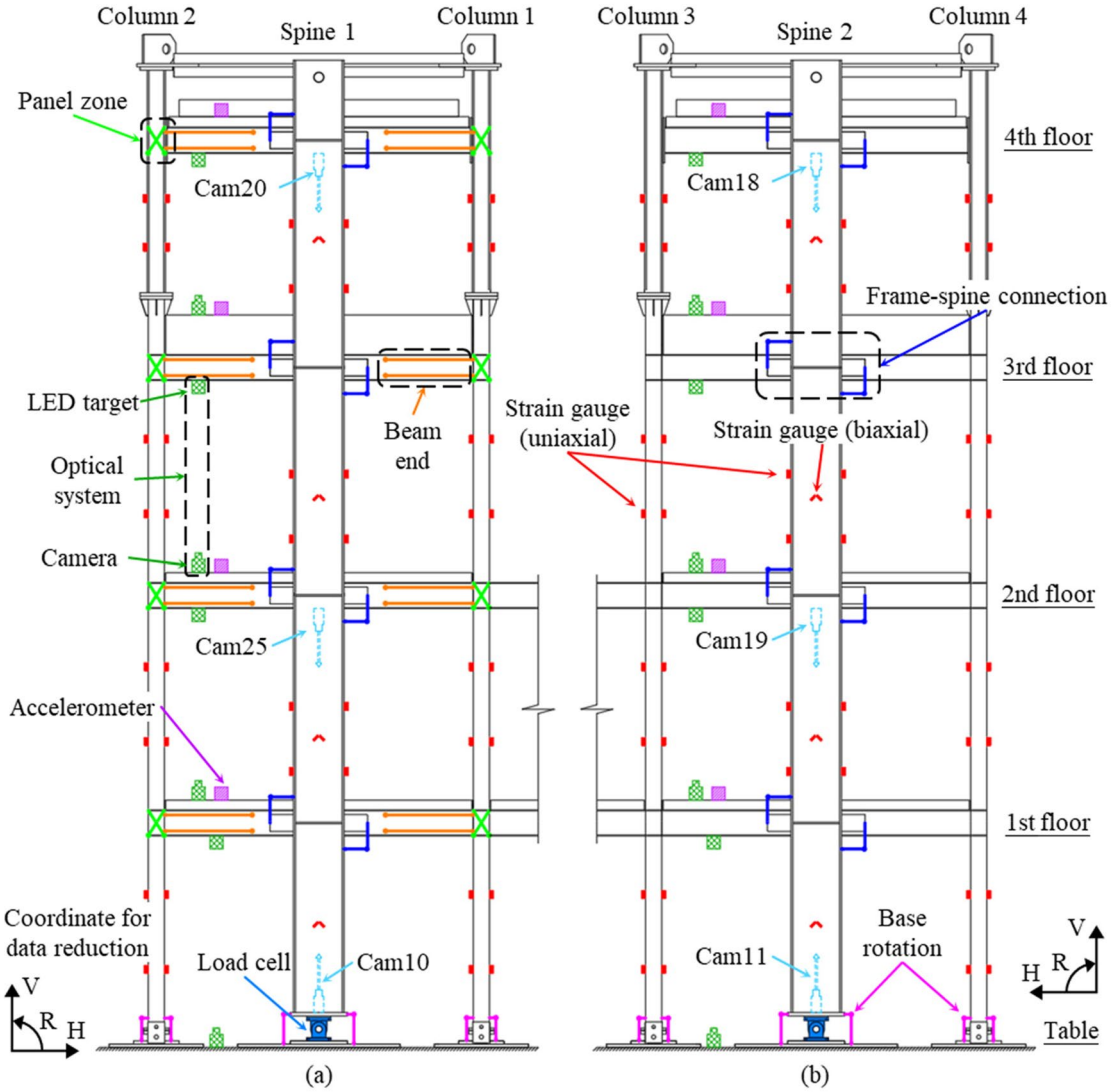

FIGURE 7 | Instrumentation scheme: (a) South elevation and (b) North elevation.

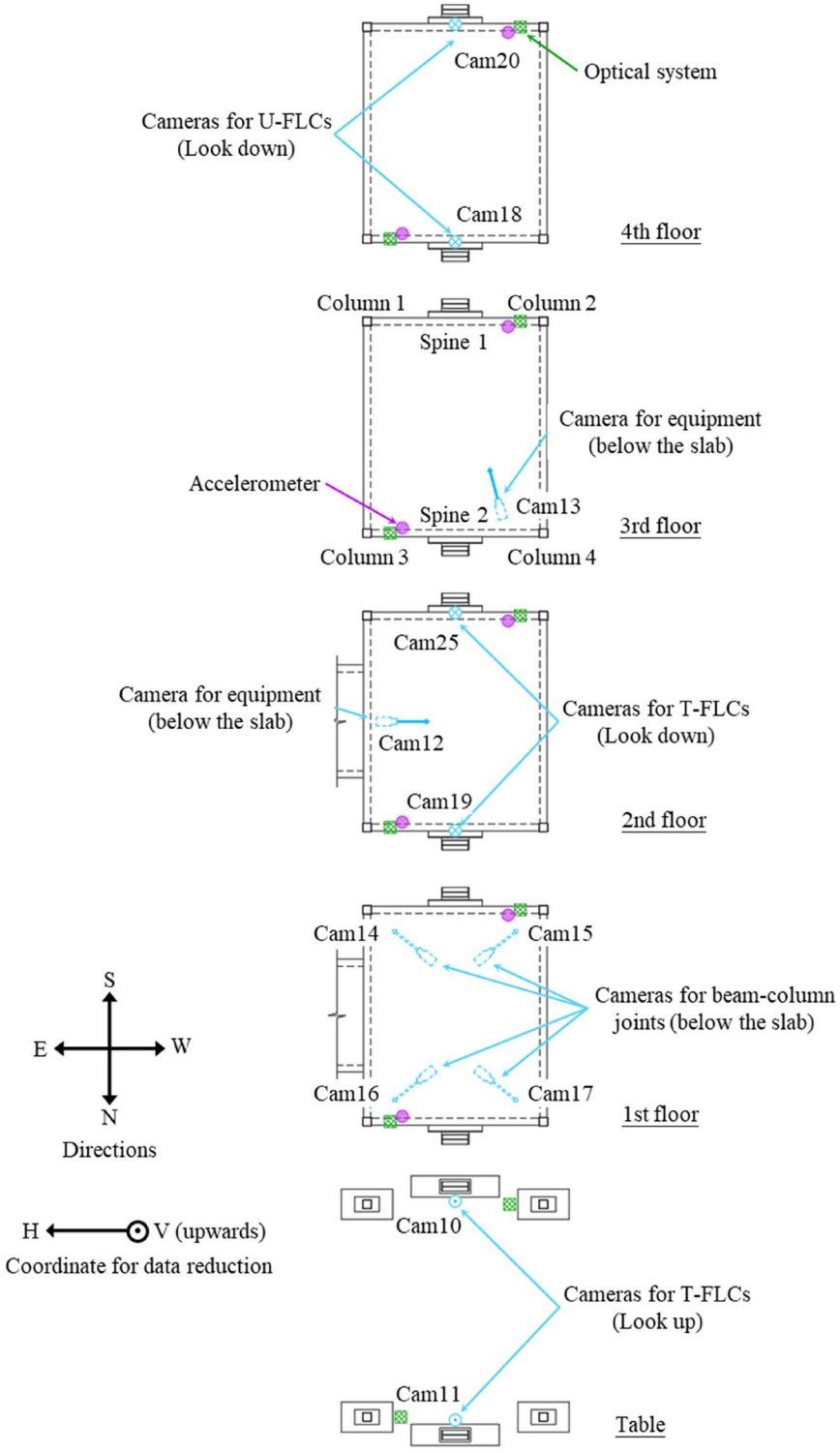

FIGURE 8 | Instrumentation scheme: floor plans.

arrangements, and Figures 10–13 illustrate the schemes to deduce physical responses.

The 6-DOF feedback signals in acceleration, velocity, and displacement used by the shake-table control system were recorded as the realized shake-table motion. These signals were used to confirm that rocking and rotation of the shake table were negligible. As shown in Figure 8, two triaxial accelerometers were placed at the diagonal opposite of each floor near the floor corners such that floor acceleration could be represented by the averaged value. Similarly, optical measurement systems were placed in pairs at each floor such that story drift could be represented by the averaged value. As shown in Figures 7a,b, 10 and 11, uniaxial and biaxial strain gauges were placed on the columns and Spines to enable deduction of internal force distribution in all MRF members. As shown in Figures 7a,b and 9a, the base pin at the Spines measured horizontal and vertical reactions. As shown in Figures 7a,b and 9h, an optical system

developed by Nishitani et al. [16] was deployed to measure the drift of each story.

As shown in Figures 7a,b, 9b, and 13a, a pair of displacement transducers were placed at each MRF-to-Spine connection to measure relative horizontal displacement. In the South frame, pairs of displacement transducers were placed to measure shear deformation of each column panel zone (see Figures 7a,b, 9c,d, and 13b) and end rotations at the ends of each beam (see Figures 7a,b, 9f,g, and 13c). As shown in Figures 7a,b, 9a,e, and 13d, a pair of displacement transducers were placed at the base pins of each Spine and column to measure base rotation.

Twenty-three video cameras were deployed to capture the global and local responses of the specimen. Camera number (Cam) 01 to 09, 28, and 31 captured the entire specimen and shake table. (Note: there were skipped camera numbers.) Figure 8 shows the locations of 12 cameras placed on the specimen, of which two (Cam 12 to 13) captured hospital equipment placed on the first and second floors, and the remaining 10 captured structural response. Figure 14 shows the views of the 10 cameras, prior to Case 01, that captured the eight FLCs (upper T-FLCs from above, lower T-FLCs from below, and pairs of U-FLCs from above), and four beam-to-column connections including column panels at the first floor.

Data from all channels and videos from all cameras were obtained from all excitations. Data were acquired by two independent systems, the data acquisition system of E-Defense that collected the majority of instruments and an optical measurement system [16] for story drift collected by Waseda University. The E-Defense data acquisition system used a sampling rate of 200 Hz, and the optical system used a sampling rate of 50 Hz. All data were initialized (set to zero) prior to Case 01, and not initialized afterward until the end.

TABLE 3 | List of instruments.

Instrument type	Brand and model	# of sensors	# of channels
Strain gauges (uniaxial)	TML FLA-5-11	88	88
Strain gauges (biaxial)	TML FCA-5-11	8	16
Linear transducer	TML SDP-50CT	4	4
	TML SDP-100CT	12	12
	TML CDP-25	16	16
Laser transducer	KEYENCE LK-500	28	28
Triaxial servo accelerometer	Tokyo Keiki TA-25E-10-1	8	24
Biaxial load cell	TOMOE	2	4
Optical system	Nishitani et al. [16]	8	16

6 | Response Deduction

Examples of schemes to deduce time-dependent physical responses are described to illustrate the use of the data. A full description of the response deduction scheme can be found in the Test Design Report provided with the data set [13]. The physical responses described below are those caused by table shaking and initialized with respect to the initial condition prior to Case 01. Initial axial forces in the first story of the four MRF columns were measured using strain data collected during

TABLE 4 | Categories of measured responses.

Targeted response		Instrument type
Floor	Floor acceleration	Triaxial servo accelerometer
Floor	Horizontal displacement	Optical system
Beam	End rotation	Linear transducer
Column panel zone	Shear deformation	Linear transducer
Spine	Base rotation	Laser transducer
Column	Base rotation	
MRF-to-Spine connection	Horizontal displacement Relative rotation	
Column	Axial force Bending moment Shear force	Strain gauges
Spine	Axial force Bending moment Shear force	Strain gauges (uniaxial)
Spine	Shear force	Strain gauges (biaxial)

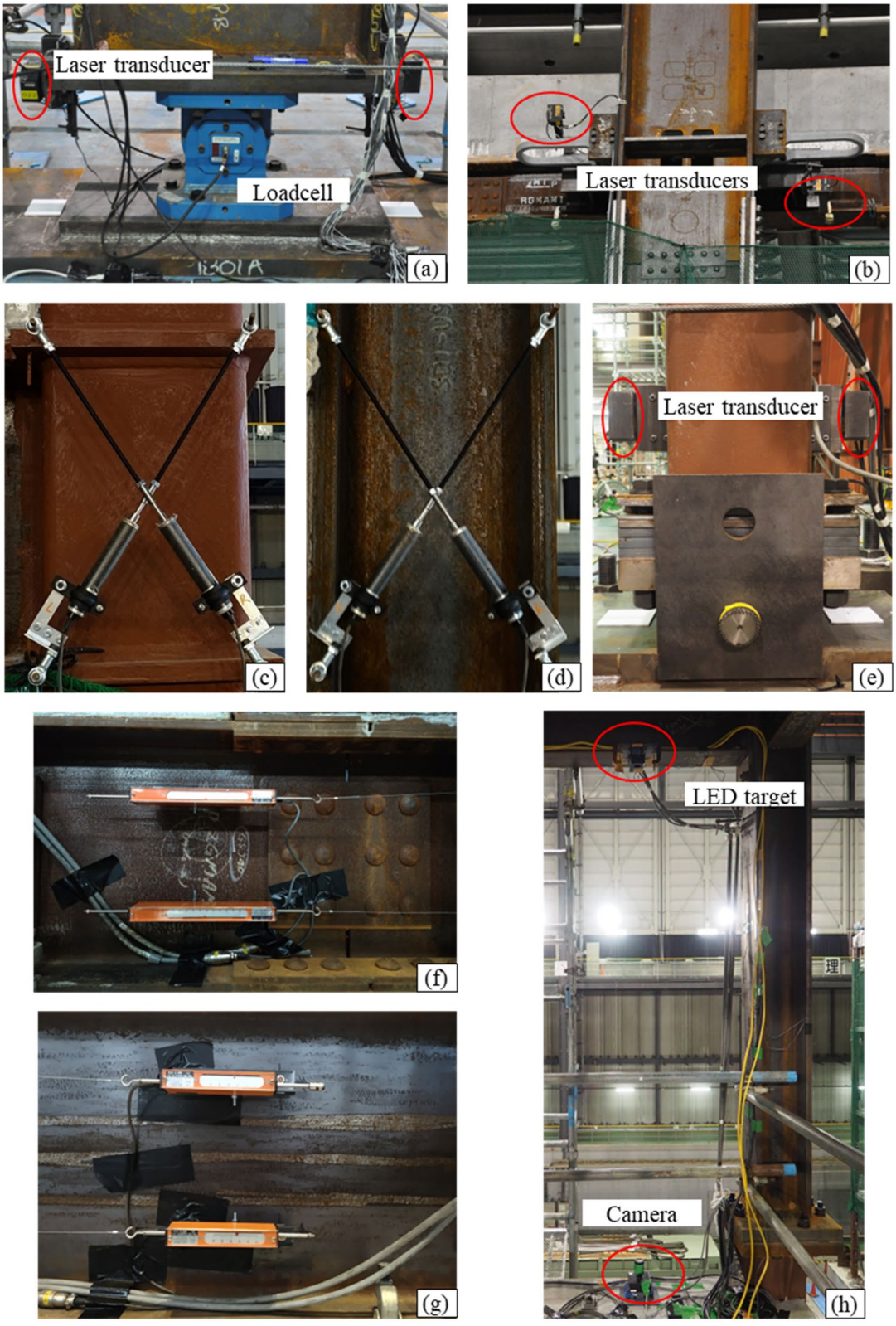

FIGURE 9 | Photos of instrumentation: (a) load cell and rotation at pinned base of Spine; (b) horizontal displacement at MRF-to-Spine connection; (c, d) shear deformation of column panel zone; (e) rotation of column base; (f, g) rotation of beam end; (h) optical system.

erection. Because the Spines were erected and connected to the MRF after the MRF was constructed on the shake table, the initial forces in the Spines are assumed to be negligible. The deduction scheme follows the *H*–*V* global coordinate system shown in Figure 1.

6.1 | Forces in Columns, Beams, and Column Panels

As illustrated in Figure 10, MRF member forces were deduced in the order of columns, beams, followed by panel zones. As shown

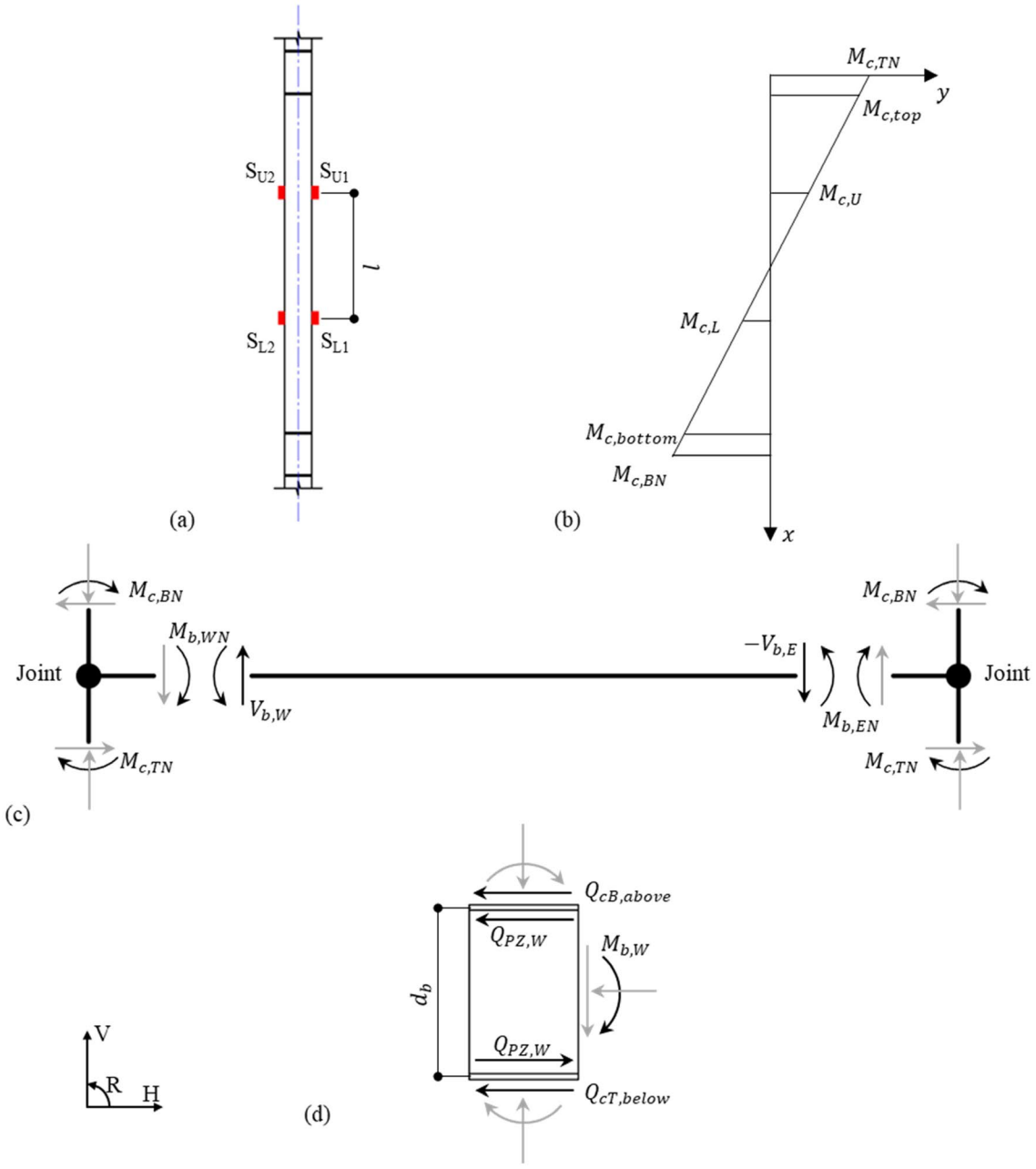

FIGURE 10 | Deduction scheme for MRF member forces: (a) strain gauges on columns; (b) column forces; (c) beam forces; (d) column-panel-zone shear force.

in Figure 10a, using strain measurement from strain gauges, axial forces, $N_{c,U}$ and $N_{c,L}$, and bending moments, $M_{c,U}$ and $M_{c,L}$, at the upper and lower instrumented sections, and shear forces, $Q_{c,T}$ and $Q_{c,B}$, at the top and bottom sections can be calculated by Equations (1–5).

$$N_{c,U} = \frac{S_{U1} + S_{U2}}{2} \cdot E \cdot A \tag{1}$$

$$N_{c,L} = \frac{S_{L1} + S_{L2}}{2} \cdot E \cdot A \tag{2}$$

$$M_{c,U} = \frac{S_{U1} - S_{U2}}{2} \cdot E \cdot Z \tag{3}$$

$$M_{c,L} = \frac{S_{L2} - S_{L1}}{2} \cdot E \cdot Z \tag{4}$$

$$Q_{c,T} = -Q_{c,B} = \frac{M_{U,C} + M_{L,C}}{l} \tag{5}$$

Here, noting member forces are defined with respect to the H–V coordinate system: S_{U1}, S_{U2}, S_{L1}, and S_{L2} are strain measurement from the uniaxial gauges indicated in Figure 10a; E is the elastic modulus of the steel, taken as $E = 2.05 \times 10^5 \text{N/mm}^2$ per Japanese design specifications [17]; A and Z are the section area and elastic section modulus, respectively, of the column, given in the Test Design Report; and l is distance between the instrumented sections, given in the Test Design Report. Noting a small

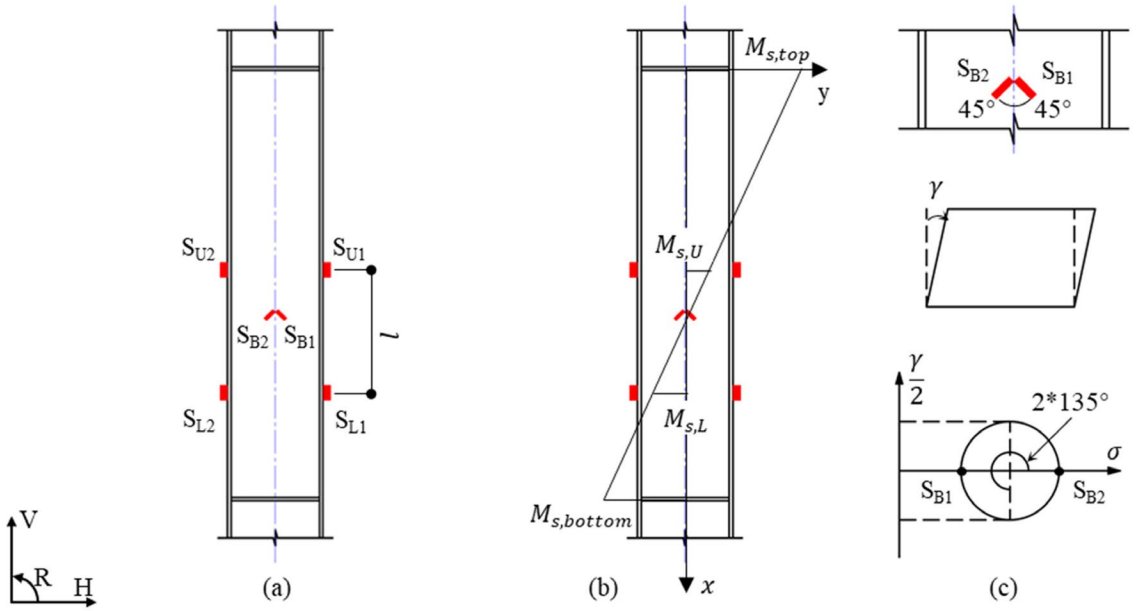

FIGURE 11 | Deduction scheme for Spine forces: (a) strain gauges on Spines; (b) deduction using uniaxial gauges; (c) deduction of shear force using biaxial gauges.

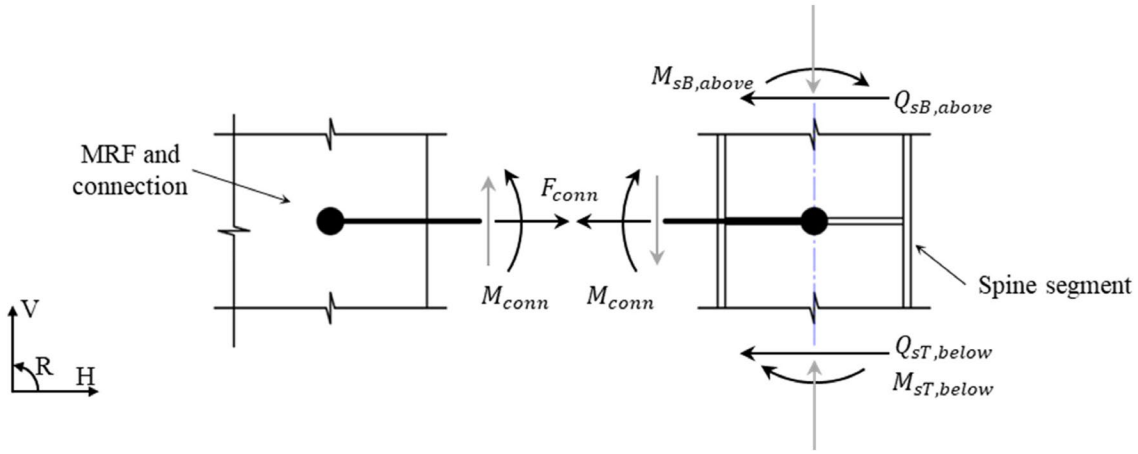

FIGURE 12 | Deduction scheme for forces in MRF-to-Spine connections.

difference between $N_{c,U}$ and $N_{c,L}$, the authors used the average of the two values to represent axial force in the column.

As shown in Figure 10b, column moments at end sections, $M_{c,top}$ and $M_{c,bottom}$, and at beam-to-column joints, $M_{c,TN}$ and $M_{c,BN}$, can be deduced via linear extrapolation using the local x–y coordinate system. As shown in Figure 10c, the beam moments at beam-to-column joints, $M_{b,WN}$ and $M_{b,EN}$, can be deduced based on equilibrium about the beam-to-column joints, and subsequently, the beam shear force, $Q_{b,W}$ and $Q_{b,E}$, and beam end moments, $M_{b,W}$ and $M_{b,E}$, can be deduced assuming linear distribution of bending moment produced by ground motion. Equations for these column and beam forces are omitted here but can be found in the Test Design Report.

As shown in Figure 10d, based on the beam and column forces, the panel-zone shear force, $Q_{PZ,W}$, for the West column panels in Columns 2 and 4 was deduced by Equation (6). A similar equation was established for the East column panel zones in Columns 1 and 3.

$$Q_{PZ,W} = -\frac{M_{b,W}}{d_b} + \frac{Q_{cB,\text{above}} - Q_{cT,below}}{2} \tag{6}$$

Here, $M_{b,W}$ is the bending moment at the west end of the beam; $Q_{cB,above}$ and $Q_{cT,below}$ are the shear forces at the bottom of the column above and top of the column below, respectively; and d_b is the center-to-center distance between the beam flanges, given in the Test Design Report.

6.2 | Deformation of Panel Zones

Figure 13b illustrates the transducers placed at the panel zones in the South frame. The shear angle, γ, of the panel zones can be deduced by Equation (7).

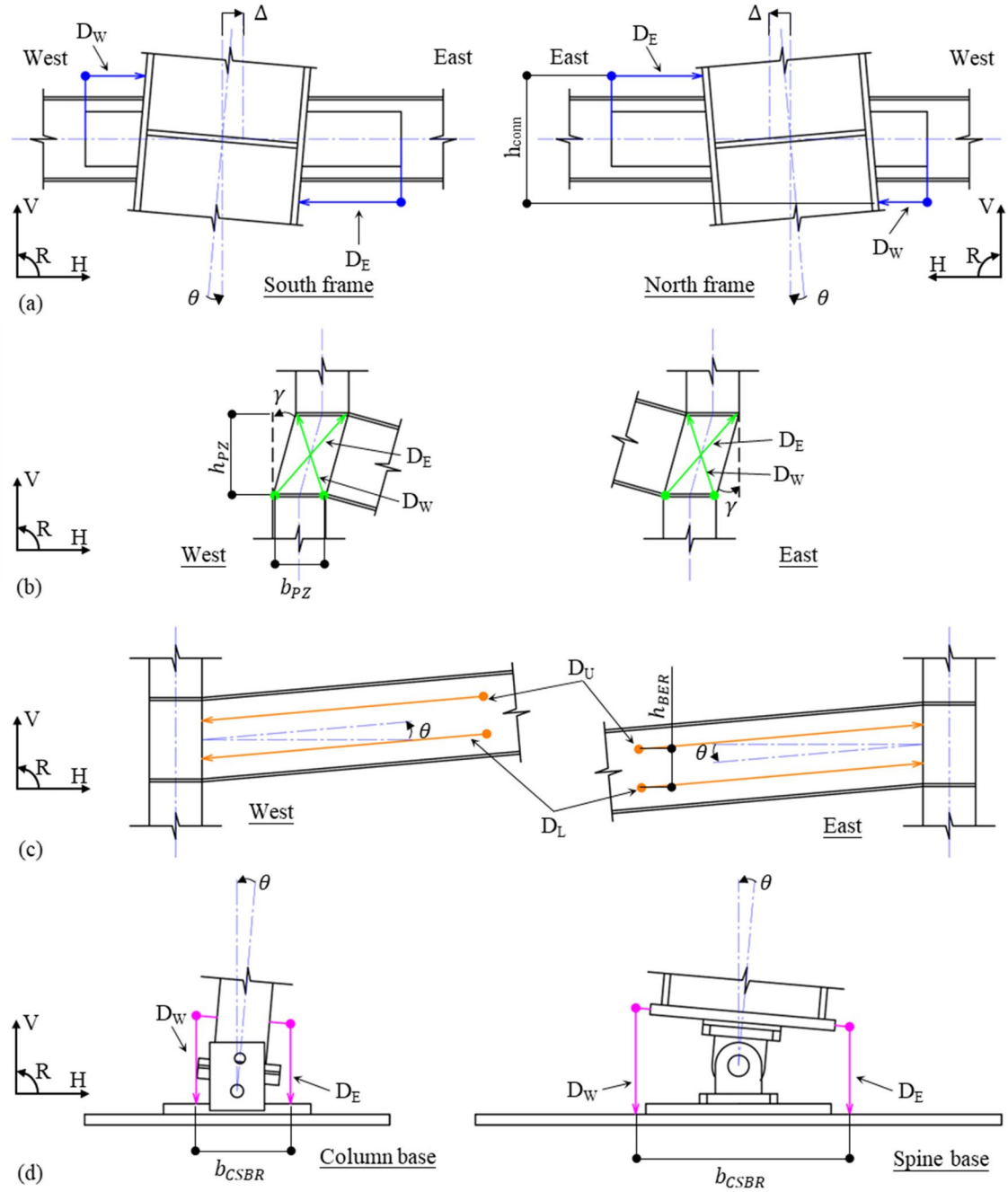

FIGURE 13 | Deduction scheme for local deformation: (a) MRF-to-Spine connection horizontal deformation; (b) column-panel-zone shear deformation; (c) beam-end rotation; (d) column and Spine base rotation. (*Note:* In (a), (b) and (d), D_E and D_W are used to indicate different transducer readings.)

$$\gamma = -\frac{1}{2}\left(\tan^{-1}\left(\frac{\sqrt{\left(l_{PZ}+D_E\right)^2-h_{PZ}^2}-b_{PZ}}{h_{PZ}}\right)+\tan^{-1}\left(\frac{-\sqrt{\left(l_{PZ}+D_W\right)^2-h_{PZ}^2}+b_{PZ}}{h_{PZ}}\right)\right) \tag{7}$$

Here, D_E is the extension measured by the lower-West to upper-East transducer; D_W is the extension measured by the lower-East to upper-West transducer; $l_{PZ}=\sqrt{b_{PZ}^2+h_{PZ}^2}$ is the diagonal length of the panel zone; and b_{PZ} and h_{PZ} are the panel width and height, respectively, given in the Test Design Report.

6.3 | Forces in Spines and MRF-To-Spine Connections

For the Spines, two independent sets of measurements can be used to deduce forces. As illustrated in Figure 11a,b, the section moments and shear forces at the second to fourth stories can be

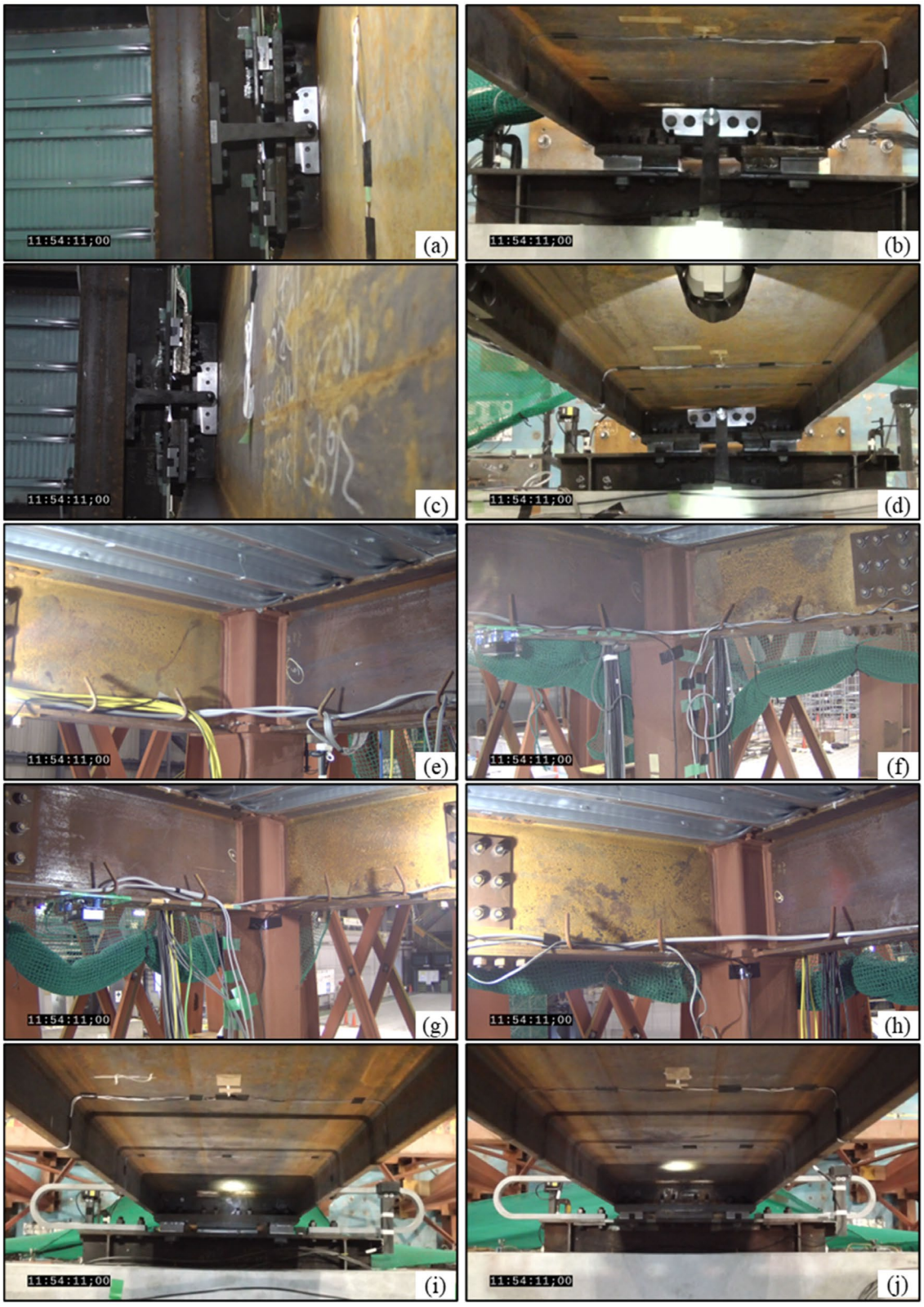

FIGURE 14 | Video camera views: (a) Cam10, Spine-1, Story 1, lower T-FLC, from below; (b) Cam25, Spine-1, Story 2, upper T-FLC, from above; (c) Cam11, Spine-2, Story 1, lower T-FLC, from below; (d) Cam19, Spine-2, Story 2, upper T-FLC, from above; (e) Cam14, Column-1, panel, Story 1; (f) Cam15, Column-2, panel, Story 1; (g) Cam16, Column-3, panel, Story 1; (h) Cam17, Column-4, panel, Story 1; (i) Cam20, Spine-1, Story 4, U-FLC pair, from above; (j) Cam18, Spine-2, Story 4, U-FLC pair, from above.

computed based on strain measurements from uniaxial strain gauges. At the first story, these forces can be obtained from reactions measured by the load cell. Independently, as illustrated by Figure 11c, the shear forces at all stories can be computed based on strain measurements from biaxial strain rosettes. The shear forces computed from the two independent schemes were

consistent with each other, although the resolution from both was compromised by the small amplitude of measured signal. (Note: the forces in the Spines were substantially smaller than their yield limit.) The former scheme using the uniaxial gauges and loadcells is recommended because the load cells provided better resolution than the measured strains, and this scheme enables deduction of all forces while the second scheme deduces only shear forces. The recommended scheme is described below.

Forces in the Spine, bending moments, $M_{s,top}$ and $M_{s,bottom}$, and shear forces, $V_{s,T}$ and $V_{s,B}$, at the top and bottom end of each story were deduced using the same methods as for column forces. Spine forces at the first story were calculated based on reactions measured by the load cells placed in the bottom pins. Finally, as illustrated in Figure 12, the horizontal force, F_{conn}, and moment, M_{conn}, transferred by the MRF-to-Spine connections can be deduced from equilibrium by Equations (8) and (9).

$$F_{conn} = -V_{sT,below} - V_{sB,above} \tag{8}$$

$$M_{conn} = -M_{sT,below} - M_{sB,above} \tag{9}$$

Here, $V_{sB,above}$ and $V_{sT,below}$ are the shear forces in the Spine above and below the connection, respectively; and $M_{s,above}$ and $M_{s,below}$ are the bending moments in the Spine above and below the connection, respectively.

6.4 | Deformation at MRF-To-Spine Connections

Figure 13a illustrates the sensors at the MRF-to-Spine connections. For both frames, the horizontal deformation, Δ, and rotation, θ, at the connections can be calculated by Equations (10) and (11). It is noted that Δ is taken positive when the Spine moves in the positive H-direction with respect to the MRF, and θ is taken positive when the Spine rotates in the positive R-direction with respect to the MRF.

$$\Delta = \frac{D_W - D_E}{2} \tag{10}$$

$$\theta = \frac{D_W + D_E}{h_{conn}} \cdot sign_{NS} \tag{11}$$

Here, D_W and D_E are the displacements measured by the West and East transducer, respectively; h_{conn} is the vertical distance between the two transducers; and $sign_{NS}$ is a factor according to the location of the connection: $sign_{NS} = -1$ at the South frame; $sign_{NS} = 1$ at the North frame.

7 | Data Postprocessing

This section describes postprocessing applied to the data prior to deducing structural responses. Details of the postprocessing can be found in the Test Design Report provided with the data set. Table 5 summarizes the postprocessing applied to each data category: acceleration, displacement, load-cell force, strain, and story drift. The postprocessing included checking for sensor failure, removing outliers (e.g., high-frequency acceleration that do not represent structural behavior, as described later; singular data points in displacement that are out of the working range of the instrument), signal filtering, compensating for failed strain gauges, and up-sampling and synchronizing between the E-Defense system and optical system (adjusting the start and end time of the latter to the former). Table 6 summarizes failed strain gauge signals noted by the authors because the gauge was stretched beyond the yield limit of the steel or because the signal was clearly unreliable. Lost signals were compensated based on a linear relationship with good signals (within, in order of preference, the same section, same column, and same story) established from earlier excitations.

TABLE 5 | Data postprocessing.

Data type	Preprocessing	Data source
Acceleration	Outlier removal	E-Defense System
	Filtering (all channels)	
Displacement	Outlier removal	
	Filtering (few channels)	
Load-cell force	Outlier removal	
	Filtering (few channels)	
Strain	Outlier removal	
	Compensation of gauges listed in Table 6	
	Filtering (few channels)	
Story drift	Up sampling (50 Hz to 200 Hz)	Waseda University
	Synchronization with E-Defense system	

Figures 15–17 illustrate examples of the postprocessing.

Figure 15 presents the raw, postprocessed, and deduced acceleration data for the first-floor accelerometer sensor data in the EW-direction from Case 09. Some subjectivity is involved in postprocessing accelerometer data [18, 19]. The plot highlights outliers that were removed prior to filtering, marked with "x" around 9.7 s. Potential outliers can be identified based on removal of double-ended jerks in the data [20] as well as comparison with the second numerical derivative of the displacement data from the optical system. While the cause of these outliers is unclear, it is seen consistently in other accelerometer signals (not shown in this figure) and occurs around yielding of the FLC. The authors suspect they resulted from impact of the FLC components or other localized effects near the sensor. Regardless, these outliers are unlikely to represent the global acceleration response of the floor mass. Outliers were removed and replaced by linear interpolation and subsequently,

TABLE 6 | Strain-gauge signal failure.

Tag	Member	Story	Location	Problem	First affected
S-B1FC1-2U	Column 1	1	Upper West	Yielded	Case 04
S-B1FC2-1U	Column 2	1	Upper East	Yielded	Case 04
S-B1FC3-2U	Column 3	1	Upper West	Yielded	Case 04
S-B1FC4-1U	Column 4	1	Upper East	Yielded	Case 04
S-B1FC3-2L	Column 3	1	Lower West	Unreliable	Case 01
S-B2FC2-2L	Column 2	2	Lower West	Yielded	Case 13
S-B2FC3-1L	Column 3	2	Lower East	Yielded	Case 13
S-B4FC1-2L	Column 1	4	Lower West	Unreliable	Case 11
S-B3FS2-2M	Spine 2	3	West Rosette	Unreliable	Case 01

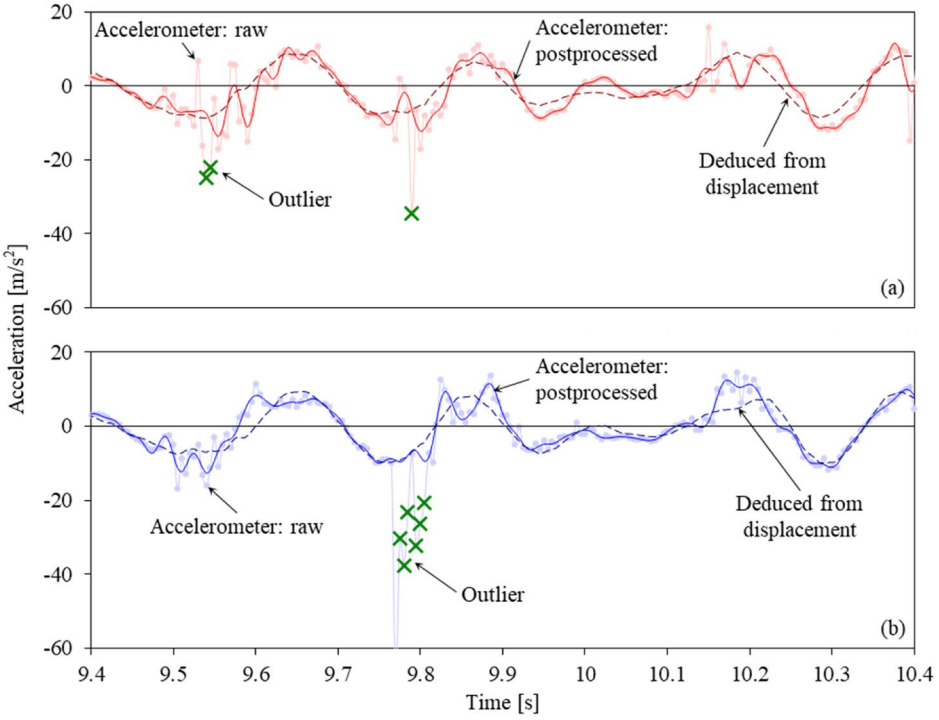

FIGURE 15 | Example of postprocessing on acceleration data (first floor, Case 09): (a) accelerometer at the South–West corner and (b) accelerometer at the North–East corner.

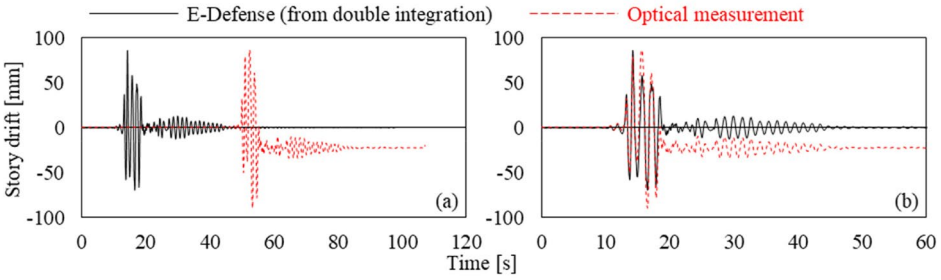

FIGURE 16 | Example of story drift synchronization shown for second story from Case 13: (a) original signals and (b) synchronized signals.

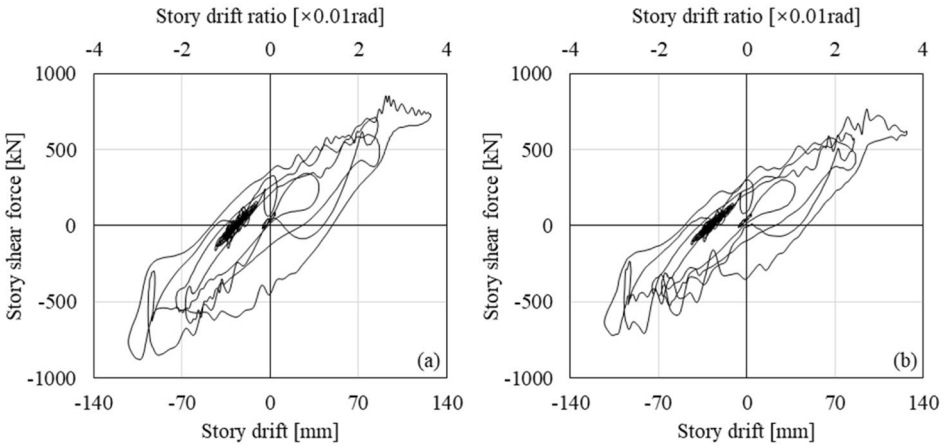

FIGURE 17 | Story shear versus story drift relationship of the first story for Case 13: (a) deduced from strains only and (b) deduced from the combination of strains and floor acceleration.

a low-pass, 20th order Butterworth filter with cutoff frequency of 35 Hz was applied to the signal. This filter was chosen not to eliminate fourth-mode response, whose frequency was no larger than 20 Hz. It is noted that, even if the outliers do not unduly affect the response history following filtering, removing multiple outliers prior to filtering can affect estimates of the peak response, affecting interpretation of effects of using the FLC. Adequacy of the process is confirmed by the good match between the postprocessed accelerations and accelerations derived from the displacement data. Accelerometer data were averaged on a per floor basis to be estimate accelerations at the center of mass.

Outlier removal was also necessary for displacement data measured by laser transducers set at the South Spine base in Case 04. A low-pass, 20th order Butterworth filter with a cutoff frequency of 20 Hz was applied to displacement data at beam ends to suppress the vibration of cables connecting the transducers and targets. A low-pass, 20th order Butterworth filter with a cutoff frequency of 35 Hz was applied to strain data from the Spines and columns in small excitations to eliminate sensor noise, which proved to be non-negligible. It should be noted that filter parameters can affect the peak responses, especially for the frequency-sensitive acceleration signals. The order of the filters was selected by trial and error and may not be suitable for all objectives, e.g., for deducing displacement by doubly integrating acceleration.

Figure 16 illustrates the scheme to synchronize signals from the optical system to that from the E-Defense data acquisition system. The second-story drift obtained from the optical system was shifted such that the start time and overall trend matched the same drift computed, merely as reference, by doubly integrating second-floor acceleration. It is cautioned that the displacement from accelerometers is shown only for reference, and that further tuning by baseline correction and choice of filtering is required to deduce displacement by double integration.

Figure 17 plots the relationship between story shear force and story drift ratio of the first story established for Case 13, which was the last of the primary excitations. The story shear force was deduced from one of two sources: from 16 strain gauges among which 5 were compensated from the other 11; and a combination of strain gauges in the second to fourth stories, 3 of which were compensated from the other many, and first-floor floor acceleration. Both sources and deduction methods resulted in similar force, although the latter resulted in smaller force and less fluctuation.

8 | Data Structure

Figure 18 illustrates the data structure. The data comprise: 01 Test design, 02 Test data, 03 FLC static tests, 04 Photos, and 05 Videos.

(01) **Test design**: This is a collection of design documents including drawings, 3D rendering data, identification for signal channels, and other introductory documents.

(01-01) **Test design report**: This folder contains a full report of the test plan including full details of the instrumentation plan and the complete data reduction scheme including essential physical distances. The report also provides initial forces under gravity loads determined from the difference in measured strain at the first story, between the lifted and set condition of the specimen, measured during erection, and linear static calculation based on assumed tributary floor areas.

(01-02) **Specimen information**: This is a collection of documents describing the specimen. Construction drawings and a 3D model of the specimen are provided. Material test results on the slab concrete and Japanese steel are also provided.

(01-03) **Excitations**: This folder summarizes target records of the excitations used in the test, including the synthetic tri-axial white noise signals, fault-normal component of the Northridge Sepulveda VA record, and N-S component of the JMA Kobe record.

(01-04) **E-Defense lists**: These lists summarize the original labeling in the E-Defense data-acquisition system for excitation cases, sensors, and cameras. The folder includes a file named

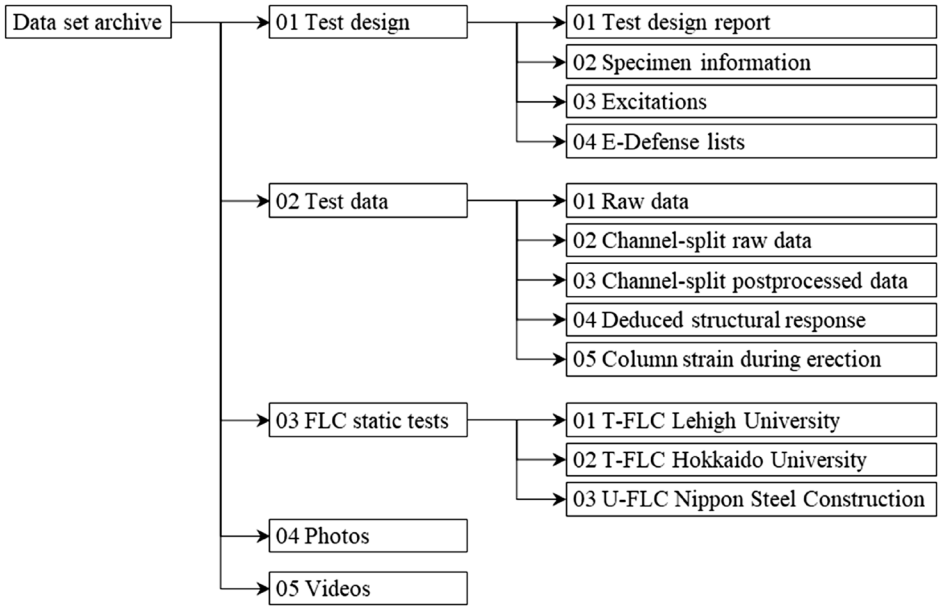

FIGURE 18 | Structure of archived data.

Sensor File that explains the calibration factors as well as the relationship between channel number, tags (according to a unified syntax), and addresses in the connection interface devices between the sensors and the E-Defense data acquisition system named unit boxes.

(02) **Test data**: This is the collection of raw signals obtained during the tests, signals after postprocessing, and structural responses deduced from the signals.

(02-01) **Raw data**: This is the original data collected by the E-Defense data acquisition system at a sampling rate of 200 Hz, and by the optical system (mentioned later) at a sampling rate of 50 Hz. The data are in physical values in units such as m/s^2, cm/s, mm, rad, micro-strain, kN, and filed according to excitation Cases 01 to 14. Data from the E-Defense data acquisition system is organized per five collection unit boxes. The only situation where users may find use of the raw data is to analyze the source of fundamental errors in data, such as mistakes in tagging and/or polarity.

(02-02) **Channel-split raw data**: This is the unprocessed data sorted to form an individual file for each channel and for each excitation. The file names are designated by channel tags and filed according to excitation cases. Errors in tagging in the raw data noted by the authors (acceleration channels A-B2F-2Y and A-B2F-2Z and column strain channels S-B1FC3-1U and S-B1FC3-2U) are corrected and documented in the Test Design Report. Users may use the channel-split raw data to examine how the plots reported by the authors were produced from individual signals after applying proper signal processing techniques.

(02-03) **Channel-split postprocessed data**: This is the postprocessed data for each channel and each excitation. The file names are designated by channel tags and filed according to excitation cases. Story drift data measured by the optical system were up-sampled from 50 Hz to 200 Hz to match the E-Defense system data, and subsequently, the data were synchronized using the scheme illustrated in Figure 16. Users may use the channel-split postprocessed data to examine how the plots reported by the authors were reproduced from individual signals and/or to examine different methodology to deduce structural responses.

(02-04) **Deduced structural responses**: This folder contains all structural responses deduced using the methods described earlier and further detailed in the Test Design Report, using postprocessed data.

(02-05) **Column strain during erection**: This folder contains strain measurements of the first-story columns during erection. These measurements can be used to obtain initial forces prior to shaking and to crosscheck with structure weight obtained from other sources.

(03) **FLC static tests**: This folder contains reports and data of static cyclic tests on the two types of FLCs used in the shake-table tests.

(03-01) **T-FLC Lehigh University**: This folder contains information on static cyclic tests of T-FLCs conducted at Lehigh University prior to the shake-table tests. The T-FLCs used in the shake table tests were identical to "Specimen 2" in these tests. Data are available in a different data set published in DesignSafe-CI [15].

(03-02) **T-FLC Hokkaido University**: This folder contains reports and data of two static cyclic tests of T-FLCs conducted at Hokkaido University after the shake-table tests. The T-FLCs used in the shake-table tests were identical to these two specimens.

(03-03) **U-FLC Nippon Steel Engineering**: This folder contains a report of static cyclic tests of U-FLCs conducted by Nippon Steel

Engineering. The U-FLCs used in the shake table tests are termed as "UD40" in these files. The source data are not disclosed.

(04) **Photos**: This is the collection of all photos taken during the shake-table test project. Photos are filed according to date starting November 7, 2020, and ending December 18, 2020, and according to category: instrumentation, local view, and global view. The specimen construction sequence, various views of the completed specimen, damage after primary excitation, and demolition and disposal sequence can be studied from the photos.

(05) **Videos**: This is the collection of test videos shot in all test cases. The cameras include fixed cameras of E-Defense and additional cameras set by the authors. All cameras were connected to the video capture system of E-Defense and thus are synchronized in time.

9 | Examples of Data Usage

Figure 19 shows the transition of modal periods of the specimen identified from the white-noise excitations. Transfer functions were deduced using the shake table feedback acceleration signal as input and floor acceleration signals as output, and peak-picking to identify these periods. It can be seen that the period stayed quite consistent between the two structural systems. The most notable elongation occurred when the FLCs were activated for all modes. Modal damping ratios identified using the half-power bandwidth method were 0.05, 0.03, 0.02, and 0.02 for the first to fourth modes, respectively.

Figure 20 illustrates the floor acceleration response history at the first floor of the MRF–Spine and MRF–Spine–FLC systems, under Northridge VA 40% and 100%. Acceleration was taken as the average of the EW-response measured by the two

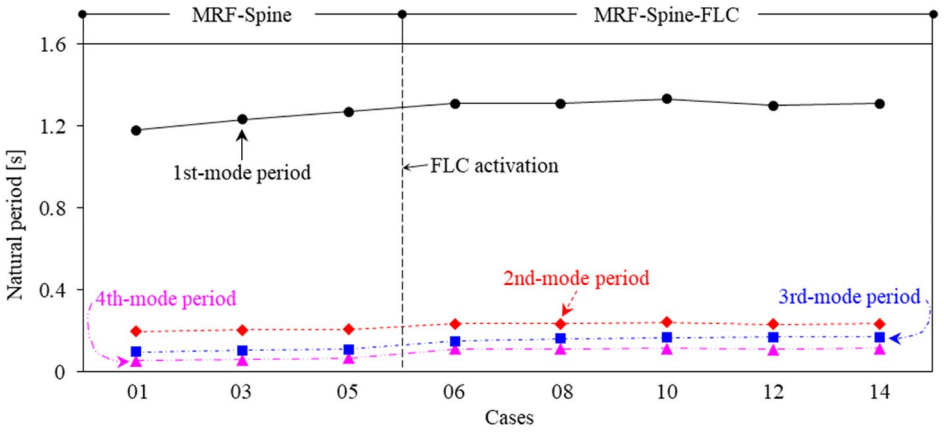

FIGURE 19 | Transition of modal periods.

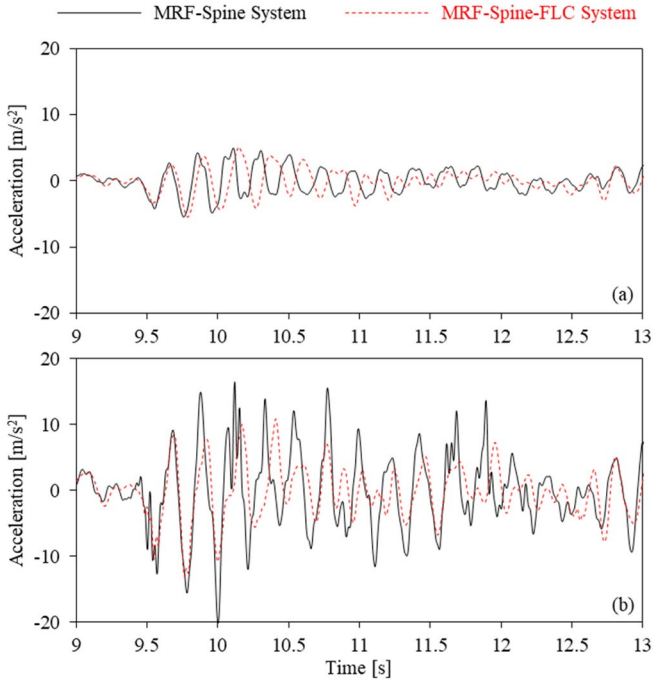

FIGURE 20 | Response history of first-floor acceleration: (a) Northridge VA 40%; (b) Northridge VA 100%.

accelerometers placed on the floor. The difference between the two systems was small under Northridge VA 40% because the MRF had not yielded and therefore the Spine was not engaged. However, the MRF–Spine–FLC system developed notably smaller floor acceleration under Northridge VA 100%, indicating the effectiveness of FLCs in controlling floor acceleration in MRFs provided with Spines. Further details of the experimental findings are reported elsewhere, for example by Fahnestock et al. [10].

Figure 21 shows the response of the West-column panel zone under JMA Kobe 100%, plotting shear force deduced by Equation (6) against shear deformation deduced by Equation (7). The figure indicates shear capacity V_p of the panel by horizontal dashed lines. The shear force exceeded the capacity, and extensive yielding occurred in the panel zone. As expected by the relative strength of MRF members, the column panel zones were a major contributor to energy dissipation.

Figure 22 shows the response of the Spine–MRF connection comprising two T-FLCs at the South frame under JMA Kobe 100%, plotting the force deduced by Equation (8) against horizontal deformation deduced by Equation (10). For reference, the figure indicates the elastic stiffness established from static cyclic tests of an isolated T-FLC. The T-FLC yielded although not extensively. The smaller stiffness compared to that from isolated static tests was likely due, in part, to the additional flexibility that was introduced through the attachment system in the full-scale building implementation.

10 | Summary

This paper introduces a data set obtained from a series of full-scale shake table tests on MRF–Spine systems with and without FLCs. The test program is described, including specimen design, instrumentation, and excitation. The data structure, methods to deduce

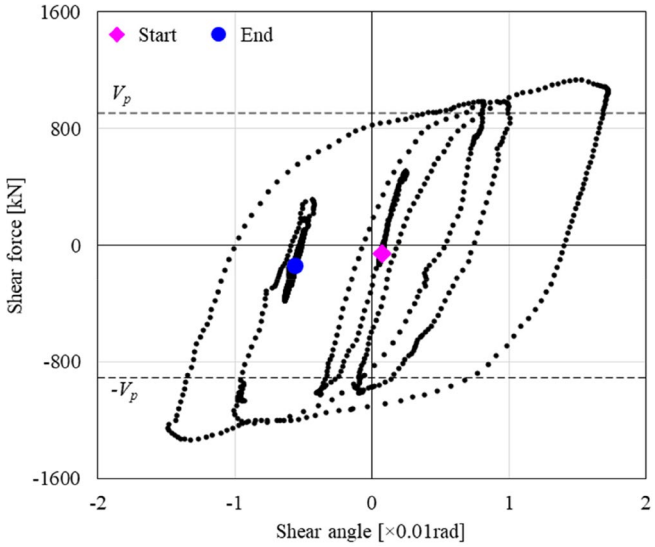

FIGURE 21 | Response of the column panel zone at the first floor of the West column under JMA Kobe 100%.

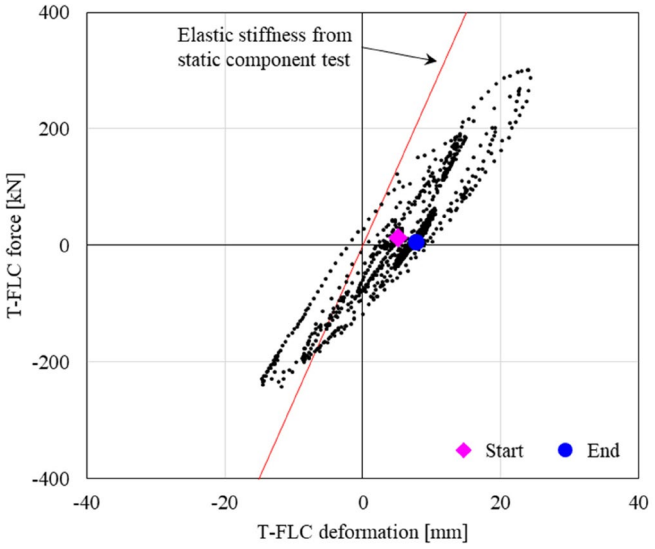

FIGURE 22 | Hysteresis of T-FLC at the South frame in the JMA Kobe 100% excitation.

response, and examples of data usage are provided. The data set introduced here provides unique, full-scale dynamic test results for a structural system with Spines. It is expected that these data can help advance the understanding of MRF–Spine–FLC systems and help formulate reliable and practical design approaches for these and similar systems. Findings from the tests have been reported so far by Fahnestock et al. [10] and Astudillo et al. [11].

Acknowledgments

The first and corresponding author was supported by the Japanese government MEXT scholarship and the Hokkaido University DX fellowship. The first and corresponding author is a member of the Architectural Institute of Japan (Membership number and Society Discount Code: 2004741). The research was funded by the U.S. National Science Foundation under the project "Collaborative Research: Frame–Spine System with Force-Limiting Connections for Low-Damage Seismic-Resilient Buildings" (CMMI 1928906, 1926326, and 1926365), the American Institute of Steel Construction, Nippon Steel, Nippon Steel Engineering Co. Ltd., Nippon Steel Metal Products Co. Ltd., the Disaster Prevention Research Institute (DPRI) at Kyoto University, JSPS KAKENHI Grant Number 20H00269, and the Tokyo Metropolitan Resilience Project of the National Research Institute for Earth Science and Disaster Resilience (NIED) (Subject C-3). Any opinions, findings, conclusions, or recommendations expressed in this paper are those of the authors and do not necessarily reflect the views of the above-mentioned funding sources.

Conflicts of Interest

The authors declare no conflicts of interest.

Data Availability Statement

The data set introduced here can be accessed via DesignSafe-CI (https://doi.org/10.17603/ds2-e159-v458). Additional information can be provided by the first author upon reasonable request.

References

1. Z. Qu, A. Wada, S. Motoyui, H. Sakata, and S. Kishiki, "Pin-Supported Walls for Enhancing the Seismic Performance of Building Structures," *Earthquake Engineering and Structural Dynamics* 41, no. 14 (2012): 2075–2091, https://doi.org/10.1002/eqe.2175.

2. T. Takeuchi, X. Chen, and R. Matsui, "Seismic Performance of Controlled Spine Frames With Energy-Dissipating Members," *Journal of Constructional Steel Research* 114 (2015): 51–65, https://doi.org/10.1016/j.jcsr.2015.07.002.

3. B. Qu, F. Sanchez-Zamora, and M. Pollino, "Mitigation of Inter-Story Drift Concentration in Multi-Story Steel Concentrically Braced Frames Through Implementation of Rocking Cores," *Engineering Structures* 70 (2014): 208–217, https://doi.org/10.1016/j.engstruct.2014.03.032.

4. J.-W. Lai and S. A. Mahin, "Strongback System: A Way to Reduce Damage Concentration in Steel-Braced Frames," *Journal of Structural Engineering* 141, no. 9 (2015): 1–11, https://doi.org/10.1061/(ASCE)ST.1943-541X.0001198.

5. R. Tremblay and L. Poncet, "Improving the Seismic Stability of Concentrically Braced Steel Frames," *Engineering Journal* 44, no. 2 (2007): 103–116, https://doi.org/10.62913/engj.v44i2.906.

6. S. Wu, P. Pan, and D. Zhang, "Higher Mode Effects in Frame Pin-Supported Wall Structure by Using a Distributed Parameter Model," *Earthquake Engineering and Structural Dynamics* 45, no. 14 (2016): 2371–2387, https://doi.org/10.1002/eqe.2766.

7. B. G. Simpson, "Higher-Mode Force Response in Multi-Story Strongback-Braced Frames," *Earthquake Engineering and Structural Dynamics* 49, no. 14 (2020): 1406–1427, https://doi.org/10.1002/eqe.3310.

8. G. Tsampras, R. Sause, D. Zhang, et al., "Development of Deformable Connection for Earthquake-Resistant Buildings to Reduce Floor Accelerations and Force Responses," *Earthquake Engineering & Structural Dynamics* 45, no. 9 (2016): 1473–1494, https://doi.org/10.1002/eqe.2718.

9. Z. Zhang, R. B. Fleischman, J. I. Restrepo, et al., "Shake-Table Test Performance of an Inertial Force-Limiting Floor Anchorage System," *Earthquake Engineering and Structural Dynamics* 47, no. 10 (2018): 1987–2011, https://doi.org/10.1002/eqe.3047.

10. L. Fahnestock, R. Sause, J. Ricles, et al., "U.S.-Japan Collaboration for Shake Table Testing of a Frame-Spine System With Force-Limiting Connections," (2021) 17th World Conference on Earthquake Engineering, 17WCEE. Sendai, Japan.

11. B. Astudillo, D. Rivera, J. Duke, et al., "Modeling Uncertainty of Specimens Employing Spines and Force-Limiting Connections Tested at E-Defense Shake Table," *Earthquake Engineering and Structural Dynamics* 52, no. 14 (2023): 4638–4659, https://doi.org/10.1002/eqe.3976.

12. E. M. Rathje, C. Dawson, J. E. Padgett, et al., "DesignSafe: New Cyberinfrastructure for Natural Hazards Engineering," *Natural Hazards Review* 18, no. 3 (2017): 1–7, https://doi.org/10.1061/(ASCE)NH.1527-6996.0000246.

13. L. Fahnestock, Y. Qie, B. Astudillo, et al., "E-Defense Shake-Table Test Data," in *Collaborative Research: Frame-Spine System With Force-Limiting Connections for Low-Damage Seismic Resilient Buildings* (DesignSafe-CI, 2025), https://doi.org/10.17603/ds2-e159-v458.

14. M. Akazawa, M. Kurata, S. Yamazaki, Y. Kawamata, and S. Matsuo, "Test and Sensitivity Analysis of Base-Isolated Steel Frame With Low-Friction Spherical Sliding Bearings," *Earthquake Engineering and Structural Dynamics* 54, no. 1 (2024): 100–118, https://doi.org/10.1002/eqe.4249.

15. J. Duncan, R. Sause, J. Ricles, L. Cao, and T. Marullo, "Coupon Material Testing," in *Collaborative Research: Frame-Spine System With Force-Limiting Connections for Low-Damage Seismic Resilient Buildings* (DesignSafe-CI, 2022), https://doi.org/10.17603/ds2-k0db-er44.

16. A. Nishitani, C. Matsui, Y. Hara, et al., "Drift Displacement Data Based Estimation of Cumulative Plastic Deformation Ratios for Buildings," *Smart Structures and Systems* 15, no. 3 (2015): 881–896, https://doi.org/10.12989/sss.2015.15.3.881.

17. AIJ (Architectural Institute of Japan), *Design Standard for Allowable Stress Design of Steel Structures* [In Japanese] (AIJ, 2019).

18. C.-Y. Seo and R. Sause, "Nonlinear Structural Response to Low-Cut Filtered Ground Acceleration Records," *Journal of Earthquake Engineering* 17, no. 8 (2013): 1212–1232, https://doi.org/10.1080/13632469.2013.814610.

19. D. A. Skolnik and J. W. Wallace, "Critical Assessment of Interstory Drift Measurements," *Journal of Structural Engineering* 136, no. 12 (2010): 1574–1584, https://doi.org/10.1061/(ASCE)ST.1943-541X.0000255.

20. D. M. Boore and J. J. Bommer, "Processing of Strong-Motion Accelerograms: Needs, Options and Consequences," *Soil Dynamics and Earthquake Engineering* 25, no. 2 (2005): 93–115, https://doi.org/10.1016/j.soildyn.2004.10.007.